J. Inst. Eng. India Ser. C (October 2020) 101(5):771–783
https://doi.org/10.1007/s40032-020-00591-6

ORIGINAL CONTRIBUTION

Dynamic Analysis of a Turbocharger Rotor-Bearing System in Transient Operating Regimes

Rajasekhara Reddy Mutra[1] · **J. Srinivas**[2]

Received: 30 July 2019 / Accepted: 5 June 2020 / Published online: 12 June 2020

Abstract This paper presents a hydrodynamic analysis of the rotor-bearing system of a high-speed turbocharger (TC) rotor supported on the floating ring bearings in transient operating conditions. By considering the temperature-dependent oil-film viscosity of lubricant and film clearances, the pressure distributions and dynamic bearing forces are calculated from the two-dimensional Reynolds equation. The dynamic behavior and stability-related issues are explained while the rotor is in start-up and shut-down conditions. The effects of various parameters including in-phase and out-of-phase unbalances at the disks on the dynamics of the overall system are studied. The generalized approach facilitates the user to select the optimum clearances and lubricant type as per the temperature rise in the system.

Keywords Finite element (FE) model · Transient analysis · Temperature-dependent viscosity · Floating ring bearings

Introduction

A turbocharger is a common platform in several modern automobiles and passenger vehicles. It is used for pressurizing the inlet air at the diffuser end with the help of expanded exhaust gases striking at the turbine end. As these turbocharger rotors are rotating at high speeds, frequent inspections are required to identify the time-to-time developed faults at various locations on the rotor. Bearings, couplings and vanes of compressor and turbine in the assembly are susceptible to several kinds of failures due to abnormal thermal and flow conditions within the casing. Often, semi or full floating ring journal bearings are used to support these high-speed rotors due to their high damping capacity and effective drag forces. Apart from synchronous vibrations occurring from rotor imbalances at low speeds of operation, sub-synchronous oscillations are also generated due to oil whip/whirl instabilities at the bearings [1]. Often the inner and outer bearing film eccentricities around the ring are maintained very low because the outer lubricant film act as a damper for the inner film whirl/whip and vice versa. As the speed increases, the oil whirl/whip instabilities are crossed and the stable-unstable limit cycle behavior is observed. Various types of sub-synchronous oscillations of the system are dictated by the stiffness of the rotor, its inertia, and the bearing parameters.

Modeling of the shaft with floating ring bearings has been illustrated with both lumped-parameter [2] and finite element models [3, 4]. Analytical, numerical and approximate techniques were found widely [5–7] to solve the Reynolds equation in flow domain. Many studies considered three-dimensional models of the rotor-bearing system for thermal and vibrational analysis. Kozhenkov and Deitch [8] described the modeling of high-velocity rotor system used in the turbochargers. A 3-D contact finite element and 2-D finite-difference approaches were used to discretize the rotor system. Zuo and Wang [9] explained an approach for the dynamic response of 3-D rotor model with uncertain factors. Suh and Palazzolo [10] implemented a three-dimensional thermo-elastic hydrodynamic model to

✉ Rajasekhara Reddy Mutra
rajmech03@gmail.com

[1] Machine Dynamics Lab, School of Mechanical Engineering, Vellore Institute of Technology, Vellore, Tamil Nadu 632014, India

[2] Department of Mechanical Engineering, National Institute of Technology, Rourkela, Odisha 769008, India

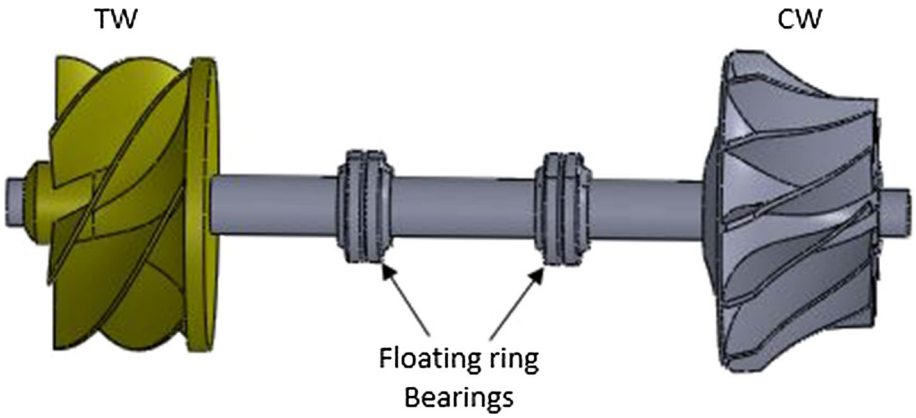

Fig. 1 Solid model of the rotor-bearing system

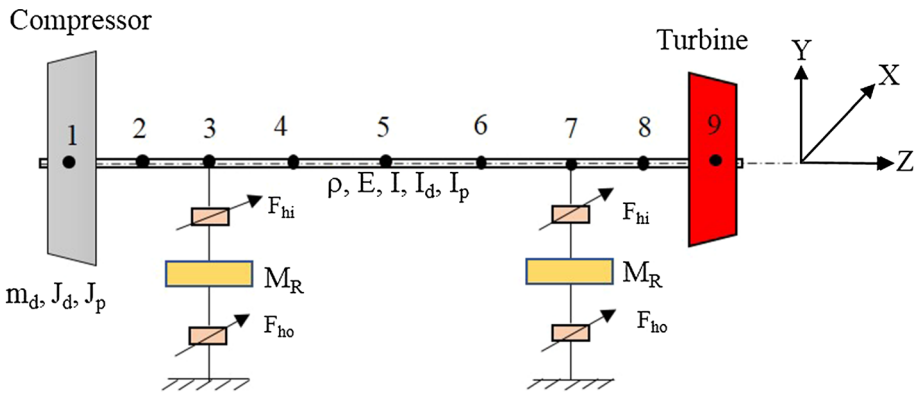

Fig. 2 Finite element model of the rotor

analyze the cylindrical pivot tilting-pad bearing system. In some studies, three-dimensional models were employed to estimate the stability and frequency characteristics of an unsymmetrical rotor-bearing system [11, 12]. Burke et al. [13] explained the modeling of automotive turbochargers for heat transfer to identify the apparent efficiency of the system. Smolik et al. [14] identified the influence of the bearing clearance in the dynamics of the turbochargers and found that by enhancing the feed pressure, there was tremendous increase in the synchronous motion amplitudes. Further, the synchronous and sub-synchronous amplitudes have dropped drastically by reducing the lubricant temperature.

The temperature of the oil may attain its flashpoint when the rotor speed reaches extremely high levels. Heat transfer and temperature field study in the thermal analysis is required not only in lubricant films but also in parts of solids which include the shaft, housing, and ring [15, 16]. In oil films, the mechanical motions and thermal behaviors are strongly coupled with the whole lubrication system. On the one hand, the bearing clearances and viscosity of the oil are strongly affected by the temperature [17–19]. Also, the heat flux is influenced by the oil-film pressure and velocity fields. Therefore, for the large speed fluid film bearings, the thermo-hydrodynamic (THD) analysis is essential. Ferron et al. [20] explained experimentally and theoretically the THD of single fluid film bearings by considering the distribution of temperature in the bush. Kadam et al. [21] explained by accounting the viscosity-temperature equation in the modified Dowson equation with the effects of THD. Durany et al. [22] explained the numerical methods to solve THD analysis for both radial and axial bearings. Here, stability, thermal effects, and turbulence were studied. For turbochargers also, the two-dimensional THD analysis was employed. At different rotational speeds, the heat distribution between the fluid film and the bearing parts was estimated [23]. Some earlier works [24, 25] explained the thermal conductivity and mass transfer of fluids. Clarke described the 2D distribution of temperature in the fluid film under the steady-state condition in the floating ring bearings [26]. Deligant et al. [27] described the power friction losses occurred due to journal bearing with the computational fluid dynamics with different lubricant entrance temperature and rotor speeds. Dhande et al. [28] proposed computational fluid dynamics to analyze pressure distribution in the three lobe hydrodynamic journal bearings. Even though many similar works are available in literature, transient dynamic behavior of such high-speed rotors with temperature-dependent bearing parameters is not studied in detail.

In the present work, dynamic analysis of a rotor-bearing system is carried out to study the influence of changes in lubricant viscosity and oil-film clearances on the overall dynamic responses. The finite element beam model of the

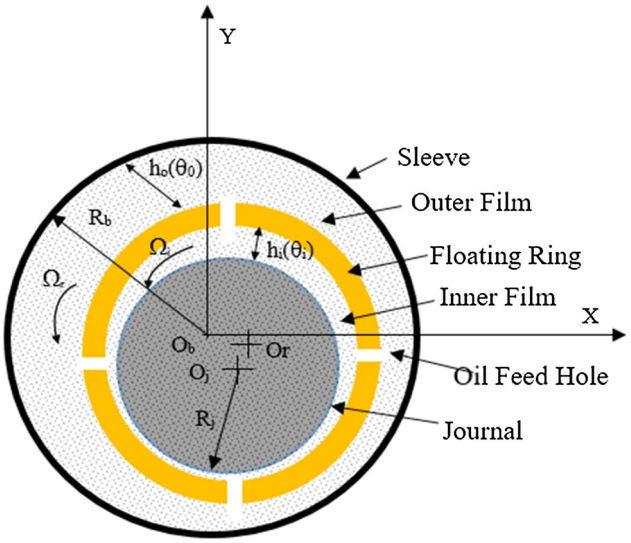

Fig. 3 Floating-ring bearing coordinate system and notation

flexible rotor system with a floating ring bearing forces is employed with consideration of nonlinear bearing forces and centrifugal effects. The free vibration solution is first validated with that of three-dimensional rotor dynamic model. By accounting the temperature-dependent viscosity and bearing clearances, a generalized framework is developed to obtain the vibration response characteristics of the rotor. The transient analysis results of the rotor revealed a significant failure patterns at certain acceleration conditions. The remaining part of the manuscript is organized as follows: section two presents the mathematical modeling of rotor-bearing system under consideration along with details of bearing film forces and transient unbalance excitations. Section three gives results and discussions, while some conclusions of the work are highlighted in section four.

Rotor-Bearing System Dynamic Model

Modeling of Rotor

The rotor assembly under consideration consists of a rotor with two disks (namely turbine wheel (TW), and compressor wheel (CW)) and bearings in its simplest form. Figure 1 shows the three-dimensional model of system assembly.

A uniform cross-section of the flexible rotor is considered, and disks are assumed as rigid. The FE beam model of the rotor-bearing system with eight elements is shown in Fig. 2 by considering the shear and bending effects.

With a convergence study, it was found that an eight element model approximates consistently the first few natural frequencies. The disks are treated as rigid lumped masses placed at the nodes one and nine, and the floating ring bearings are placed at the nodes three and seven. Every node has 4 degrees of freedom (DOF) which includes two bending deflections (υ_x, υ_y) and corresponding slopes (φ_x, φ_y). Effect of shear deformation is considered during modeling. The equations of motion of the rotor system are written as:

$$\left[\hat{M}_s\right]\{\ddot{\hat{q}}_e\} + \left[\left[\hat{C}_s\right] + \left[\hat{G}_s\right]\right]\{\dot{\hat{q}}_e\} + \left[\hat{K}_s\right]\{\hat{q}_e\} = \{F_u\} + \{\mathrm{Fh}_{\mathrm{inner}}\} \quad (1)$$

where $\left[\hat{M}_s\right]$ is rotor mass matrix, $\left[\hat{C}_s\right]$ is damping matrix, $\left[\hat{G}_s\right]$ and $\left[\hat{K}_s\right]$ are, respectively, gyroscopic and stiffness matrices, $\{\hat{q}_e\}$ is the vector displacement, $\{F_u\}$ is the gravity and unbalance force vector at the disks which have a phase difference (ϕ) between two disks, and $\{\mathrm{Fh}_{\mathrm{inner}}\}$ is the inner lubricant film hydrodynamic force. As the slopes cannot be measured experimentally, they are treated as slave or secondary degrees of freedom and are eliminated using dynamic condensation scheme [29]. The reduced stiffness, mass and gyroscopic matrices are further employed. The equations of motion for the floating rings in two bearings are written as:

$$[\hat{M}_{\mathrm{R}}]\{\ddot{\hat{q}}_{\mathrm{R}}\} = \{\mathrm{Fh}_{\mathrm{outer}}\} - \{\mathrm{Fh}_{\mathrm{inner}}\} \quad (2)$$

where $\{q_R\}$ denotes the floating ring displacement vector, $[\hat{M}_R]$ is the effective 4×4 size ring mass matrix corresponds to the two bearings. $\{Fh_{\mathrm{outer}}\}$, $\{Fh_{\mathrm{inner}}\}$ are two lubricant exciting force vectors. Since there is a relative motion between the journal and floating ring, the assembled system of equations is eventually represented as:

$$\begin{bmatrix} [\hat{M}_s] & [0] \\ [0] & [\hat{M}_R] \end{bmatrix} \begin{Bmatrix} \ddot{U} \\ \ddot{U}_R \end{Bmatrix} + \begin{bmatrix} [\hat{C}_s] & [0] \\ [0] & [0] \end{bmatrix} \begin{Bmatrix} \dot{U} \\ \dot{U}_R \end{Bmatrix} + \begin{bmatrix} [\hat{K}_s] & [0] \\ [0] & [0] \end{bmatrix} \begin{Bmatrix} U \\ U_R \end{Bmatrix} = \{F\} \quad (3)$$

where U and U_R are the shaft nodal displacement vector and floating ring degrees of freedom vector, respectively.

Table 1 The geometry of the rotor and bearings [33]

Parameter	Value
Outer diameter of turbine wheel (mm)	50
Outer diameter of compressor wheel (mm)	55
Journal diameter (mm)	15
Bearing inner diameter (mm)	15
Bearing outer diameter (mm)	25
Ring mass (gm)	7.2
Ring polar moment of inertia (kg-mm^2)	33.641

Forces in Floating Ring Bearing

A floating ring bearing consists of a ring, which is placed between the rotating journal and fixed sleeve. The ring consists of feed holes through which the oil is circulated from inner film to outer film. As the floating ring divides the lubricant film into inner and outer parts, the forces acting on the ring from the outer surface are relative values of the outer $\{F_{\text{outer}}\}$ and inner $\{F_{\text{inner}}\}$ forces. The total force vector $\{F\}$ with an unbalance load at the two disks $\{F_u\}$ is given as follows.

$$\{F\} = \begin{bmatrix} \{F_u\} \\ \{0\} \end{bmatrix} + \begin{bmatrix} \{F_{\text{inner}}\} \\ \{F_{\text{outer}} - F_{\text{inner}}\} \end{bmatrix} \tag{4}$$

The coordinate system on the bearing along with important parameters is shown in Fig. 3.

The system dynamics depends on the ring-to-shaft speed ratio, lubricating oil viscosity, and the bearing clearances. The Reynolds equations with transient terms for the both (inner and outer) films can be expressed as:

$$\frac{1}{R_{\text{jo}}^2}\frac{\partial}{\partial\theta_{\text{in}}}\left(\frac{h_{\text{in}}^3}{12\mu_{\text{in}}}\frac{\partial p_{\text{in}}}{\partial\theta_{\text{in}}}\right) + \frac{\partial}{\partial z_{\text{ni}}}\left(\frac{h_{\text{in}}^3}{12\mu_{\text{in}}}\frac{\partial p_{\text{in}}}{\partial z_{\text{in}}}\right) = \frac{\Omega_{\text{jo}} + \Omega_{\text{rn}}}{2}\frac{\partial h_{\text{in}}}{\partial\theta_{\text{in}}} + \frac{\partial h_{\text{in}}}{\partial t} \tag{5}$$

$$\frac{1}{R_{\text{ro}}^2}\frac{\partial}{\partial\theta_{\text{ou}}}\left(\frac{h_{\text{ou}}^3}{12\mu_{\text{ou}}}\frac{\partial p_{\text{ou}}}{\partial\theta_{\text{ou}}}\right) + \frac{\partial}{\partial z_{\text{ou}}}\left(\frac{h_{\text{ou}}^3}{12\mu_{\text{ou}}}\frac{\partial p_{\text{ou}}}{\partial z_{\text{ou}}}\right) = \frac{\Omega_{\text{ri}}}{2}\frac{\partial h_{\text{ou}}}{\partial\theta_{\text{ou}}} + \frac{\partial h_{\text{ou}}}{\partial t} \tag{6}$$

where the subscripts *in* and *ou* represent the parameters of the inner and outer oil films, respectively. The subscripts *jo* and *r*, respectively, indicate the parameters for the journal and floating ring. Also, μ is the lubricant viscosity and p refers to oil-film pressure. The radii of journal and floating ring are represented as R_j and R_{ro}, respectively, and h_{in} and h_{ou}, respectively, denote the inner and outer oil-film thicknesses. Simplifying and solving the equations with short bearing approximation under appropriate boundary conditions, the oil-film force components derived from pressure distributions are explicitly expressed as [30]:

Table 2 Modal frequencies comparison (Hz)

Natural frequency	1-D beam analysis	3-D Ansys solution
First	1267.4	1270.6
Second	2116.4	2136.0
Third	4145.1	4376.2
Fourth	5092.2	5106.6
Fifth	6450.7	6470.8
Sixth	6845.5	6867.3

$$\begin{Bmatrix} F_{\text{inner}-x} \\ F_{\text{inner}-y} \end{Bmatrix} = \mu_{\text{in}}(\Omega_{\text{jo}} + \Omega_{\text{rn}})R_{\text{jo}}L_{\text{in}}\left(\frac{R_{\text{jo}}}{C_1}\right)^2\left(\frac{L_{\text{in}}}{2R_{\text{jo}}}\right)^2\begin{Bmatrix} f_{\text{inner}-x} \\ f_{\text{inner}-y} \end{Bmatrix} \tag{7}$$

$$\begin{Bmatrix} F_{\text{outer}-x} \\ F_{\text{outer}-y} \end{Bmatrix} = \mu_{\text{ou}}\Omega_{\text{rn}}R_{\text{ro}}L_{\text{ou}}\left(\frac{R_{\text{ou}}}{C_2}\right)^2\left(\frac{L_{\text{ou}}}{2R_{\text{ro}}}\right)^2\begin{Bmatrix} f_{\text{outer}-x} \\ f_{\text{outer}-y} \end{Bmatrix} \tag{8}$$

Also, the journal and bearing component forces are represented as $f_{\text{inner-}x}$, $f_{\text{inner-}y}$, and $f_{\text{outer-}x}$, $f_{\text{outer-}y}$, respectively.

Temperature-Dependent Bearing Parameters

In practice, during turbocharger operation, the oil-film viscosity and clearances vary as a function of temperature. In the present analysis, the viscosity of lubricant μ is considered as an exponential function of temperature T for both (inner and outer) films [31] and is expressed as:

$$\mu = \mu_\infty - \left[\frac{\mu_\infty - Ke^{\frac{c}{(d+T)}}}{\left[\frac{\dot{\zeta}}{\dot{\zeta}_i}\right]}\right] \tag{9}$$

where μ_∞ denotes the viscosity reference value at a null shear rate, while K, c and d are Vogel's viscosity fitting parameters selected from experimentally tabulated data. The symbol $\dot{\zeta}$ is the shear rate and $\dot{\zeta}_i$ is the shear rate that produces 50% reduction in reference viscosity, respectively.

Transient Dynamic Forces

The components of unbalance forces at the two disks under non-uniform speeds are given by:

$$F_{u1x} = m_1e_1\omega^2\cos(\omega t) + m_1e_1\alpha\sin(\omega t) \tag{10}$$

$$F_{u1y} = m_1e_1\omega^2\sin(\omega t) - m_1e_1\alpha\cos(\omega t) \tag{11}$$

$$F_{u2x} = m_2e_2\omega^2\cos(\omega t + \varphi) + m_2e_2\alpha\sin(\omega t + \varphi) \tag{12}$$

$$F_{u2y} = m_2e_2\omega^2\sin(\omega t + \varphi) - m_2e\alpha\cos(\omega t + \varphi) \tag{13}$$

where e_i (i = 1, 2) are disk unbalance eccentricities, ω and α are the steady-state angular speed and angular acceleration of the system, while ϕ is the phase angle between the disks. All the above unbalance force components along with nonlinear bearing forces are incorporated into the assembled systems of finite element equations. To obtain the time-dependent unbalance responses, the resultant coupled system of equations of the shaft and bearing are solved numerically by fourth-order Runge–Kutta explicit time integration scheme [32].

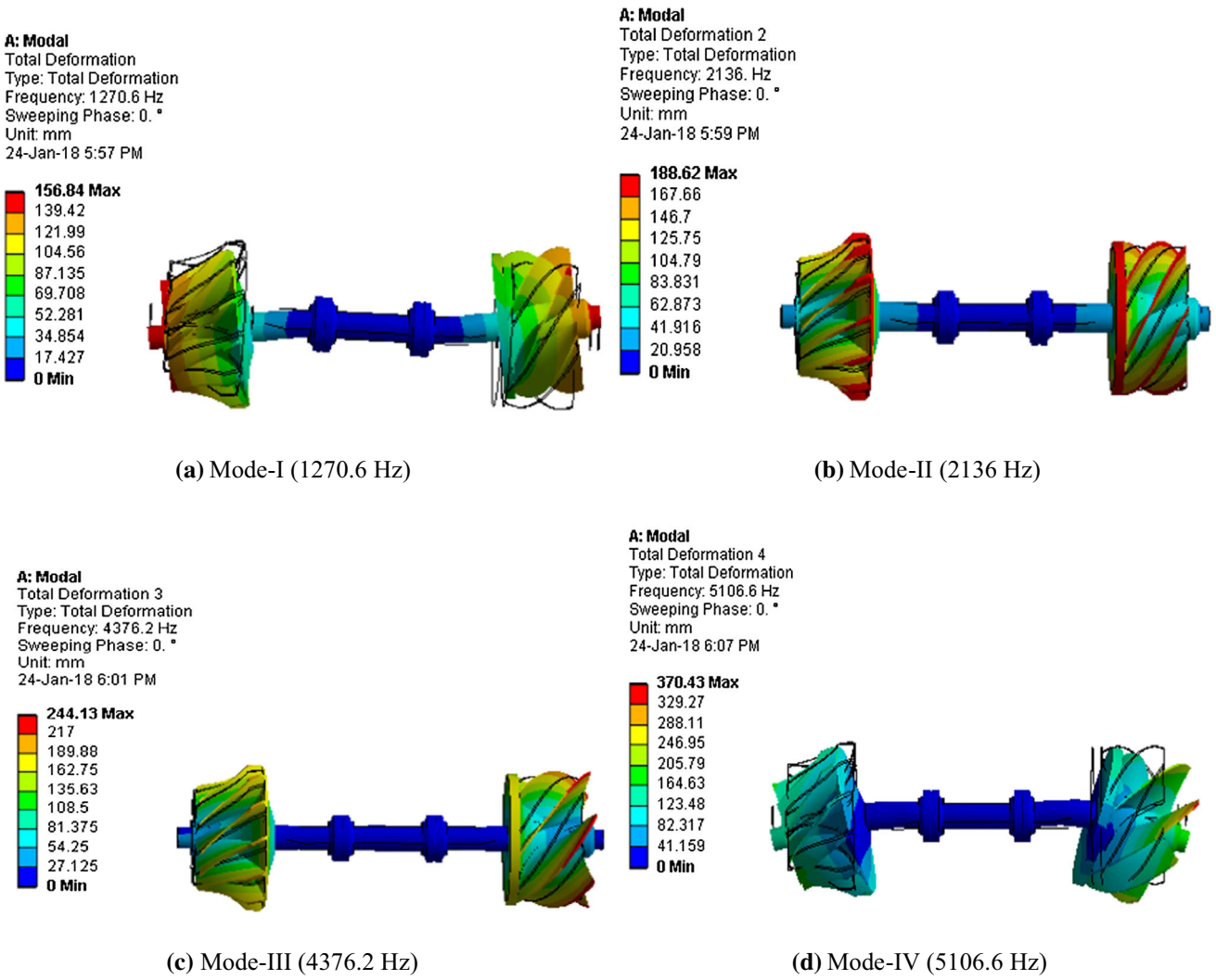

(a) Mode-I (1270.6 Hz) **(b)** Mode-II (2136 Hz)

(c) Mode-III (4376.2 Hz) **(d)** Mode-IV (5106.6 Hz)

Fig. 4 Mode shapes of the Turbocharger

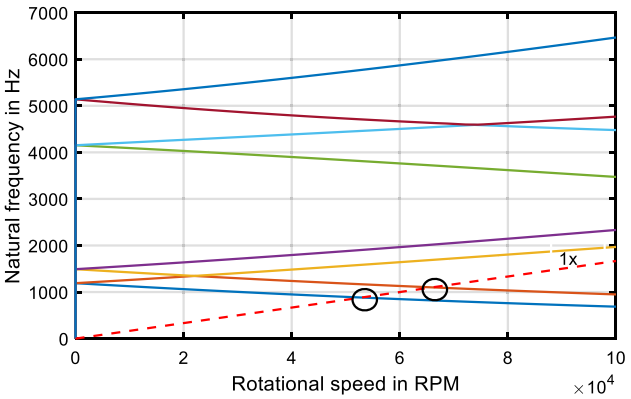

Fig. 5 Campbell diagram

Results and Discussion

Initially, three-dimensional analysis of the TC rotor model is performed. The specifications of the shaft and bearing systems considered are shown in Table 1.

The diameters of the turbine (Titanium alloy) and a compressor wheel (Aluminum alloy) are considered as 50 mm and 55 mm, respectively. The total span of the shaft is 155 mm, and the mass of the both disks (compressor and turbine) is taken as 0.118 kg and 0.326 kg. Three-dimensional analyses are conducted in ANSYS 15.0 software by meshing the rotor unit using 8-node SOLID187 elements. All the nodal degrees of freedom along the outer sleeves of the bearings are constrained, and the appropriate properties of the bearings are selected [34].

An in-house code is also developed in MATLAB for finding the assembled stiffness, mass and gyroscopic matrices of Timoshenko beam elements which idealize the rotor system. With lumped masses and inertias at the disk nodes along with disk gyroscopic matrices, the free vibration solutions are obtained at different speeds of operation. First six matching frequencies of the rotor in non-rotating state are shown in Table 2.

Table 3 Operating parameters of oil films [14]

Side	Lubricant film	Clearance nominal/hot (mm)	Temperature (°C)	Viscosity (Centi-Poise)
Turbine	Inner film	0.015/0.018	180	4.9
	Outer film	0.033/0.024	140	8.9
Compressor	Inner film	0.015/0.019	130	6.4
	Outer film	0.033/0.025	120	8.4

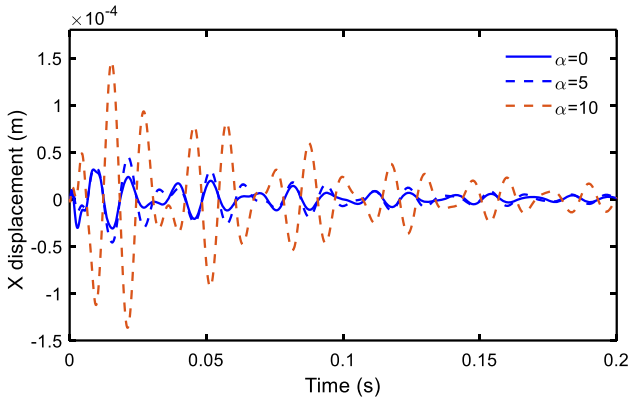

(a) X-direction

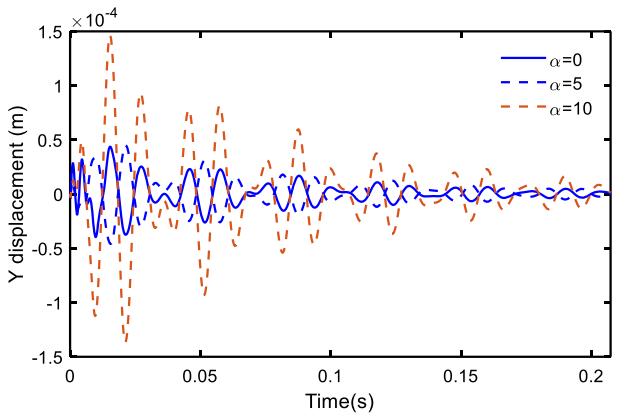

(b) Y-direction

Fig. 6 Time domain response at the left bearing

It is seen that the frequencies are very closely matching. The corresponding four mode shapes as obtained from 3-D analysis are illustrated in Fig. 4.

It is seen that the first two mode shapes are conical, while the last two are translational in nature. In the above study, the bearings are treated with linear spring elements. Figure 5 represents the Campbell plot of the system indicating the critical speeds of operation. It can be identified that the first two critical speeds are approximately 49 krpm and 62 krpm.

Table 3 shows the clearances and viscosity of lubricant considered for the two floating ring bearings. The nominal conditions for the lubricant are taken at room temperature. Due to varying temperature conditions inside the bearing and material dissimilarities, the operating clearances are different from nominal ones.

The stability issues and sub-synchronous responses are explained while the rotor is accelerating/decelerating to a steady speed. Speed of the rotor is considered to change from rest to 10,000 rpm. The angular acceleration (α) influence on the vibration response is studied. Figure 6 shows the unbalance response at the left bearing node for various levels of angular accelerations α.

It is seen that as the angular acceleration increases, the vibration amplitudes increase particularly in lower time regions. The corresponding journal trajectories at the left bearing node are shown in Fig. 7, indicating the whirl motion of the journal within the floating ring inner annulus.

It is seen that the motion is well within the ring at these operating conditions. Figure 8 shows the unbalance response at the left bearing node as the rotor decelerates uniformly. It is seen that the amplitudes reduce with deceleration magnitudes.

Further, an experimental study is conducted on the automotive turbocharger rotor. The dynamic response is measured at the left bearing as the rotor speed uniformly goes from zero to 1000 rpm in 5 s. Figure 9 shows the experimental setup considered for testing. For the response measurements, an IPO type accelerometer (1–10 kHz) with a charge amplifier is used.

Tektronix model DPO 43034, a four-channel digital oscilloscope, is used to record the time history during the transient period. A variable speed drive is used to increase/decrease the rotor speed. Figure 10 shows the experimentally measured time-response (acceleration) and corresponding FFT diagram as the rotor accelerates from zero to 1000 rpm. It is seen that the pulsing peaks are developed during the speed change, indicating the crossing of critical speeds.

Figure 11 shows the time history and frequency response when decelerating from 1000 rpm to null speed.

It is observed that while decelerating, the amplitudes are reducing and the sub-synchronous peak frequencies in FFT are coinciding with those of accelerating case. Both the accelerating and decelerating cases are studied numerically using the present program with the above operating

Fig. 7 Orbit plot at left bearing

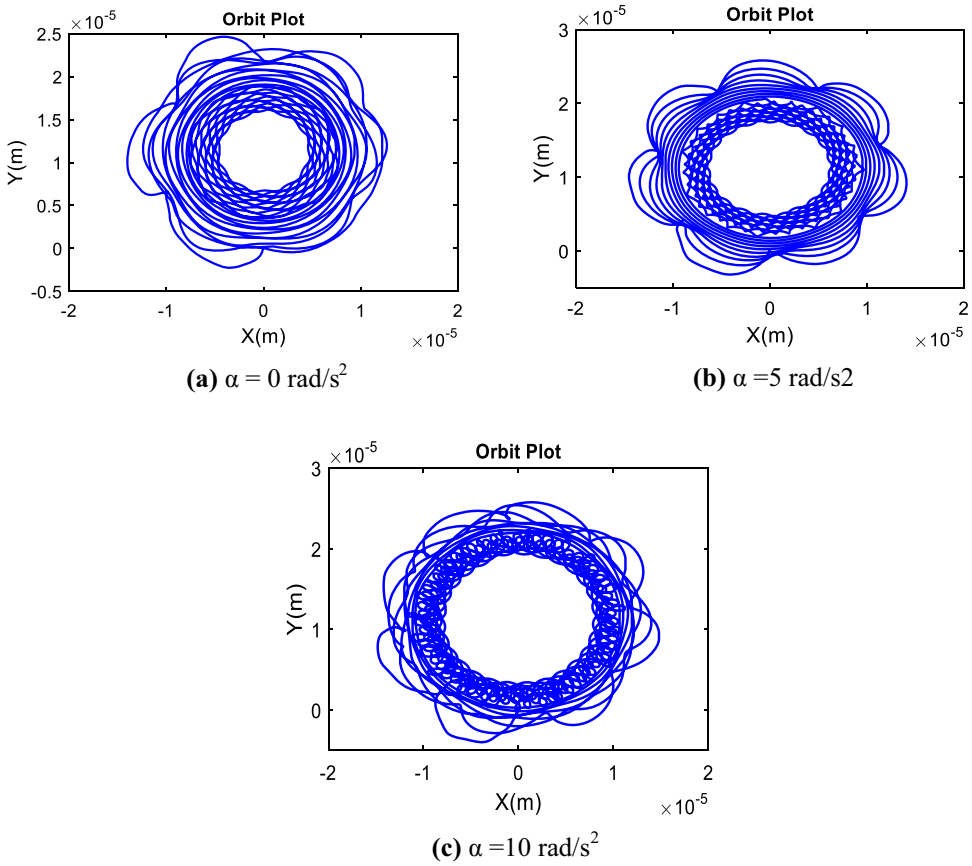

(a) α = 0 rad/s^2 **(b)** α =5 rad/s2

(c) α =10 rad/s^2

Fig. 8 Time-domain response at the left bearing

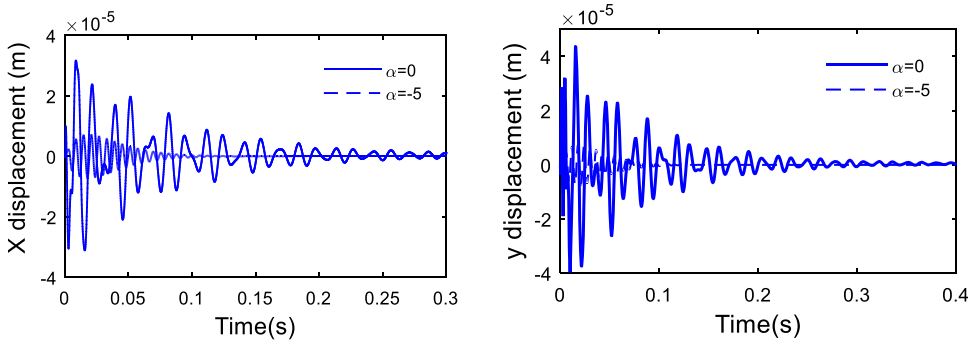

(a) X-direction **(b)** Y-direction

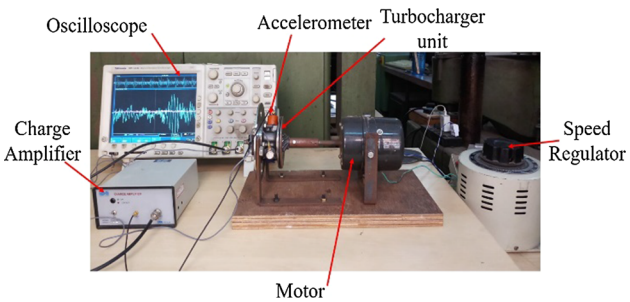

Fig. 9 Experimental setup

acceleration/deceleration. Figures 10c and 11c indicate the FFT of the responses at left bearing node for both cases obtained numerically. It is seen that there are three dominant peak frequencies from experiment occurring at 29 Hz, 85 Hz and 268 Hz, respectively, as shown in Fig. 10b. Figure 10c shows transient response obtained from the present FE model, which possesses the dominant frequencies nearly as 28.69 Hz, 87.28 Hz and 266.7 Hz. Similarly, during deceleration, the three dominant peak frequencies in transient response are noticed at 29 Hz, 75 Hz and 268 Hz, respectively, in experimental acceleration curve, while these are found at 27.47 Hz, 75.07 Hz and 266.7 Hz, respectively, through the present FE simulations as seen

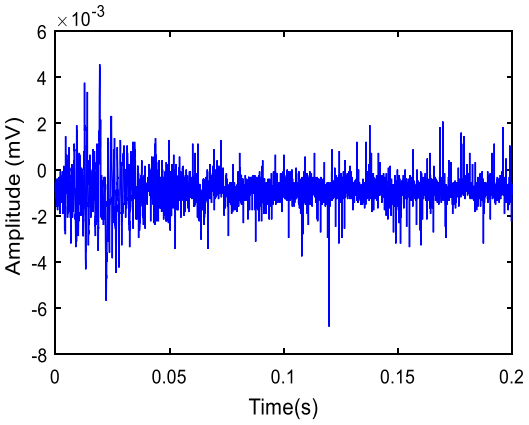

(a) Time history

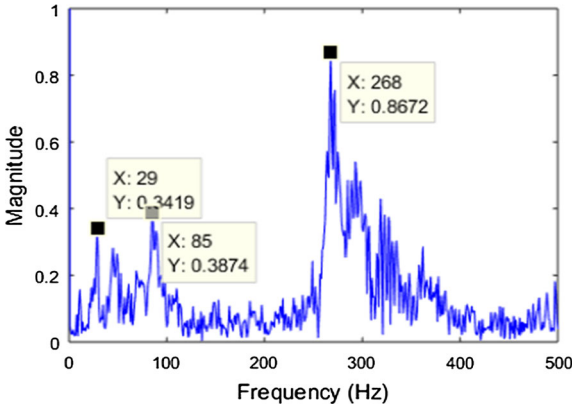

(b) Frequency response from experimental

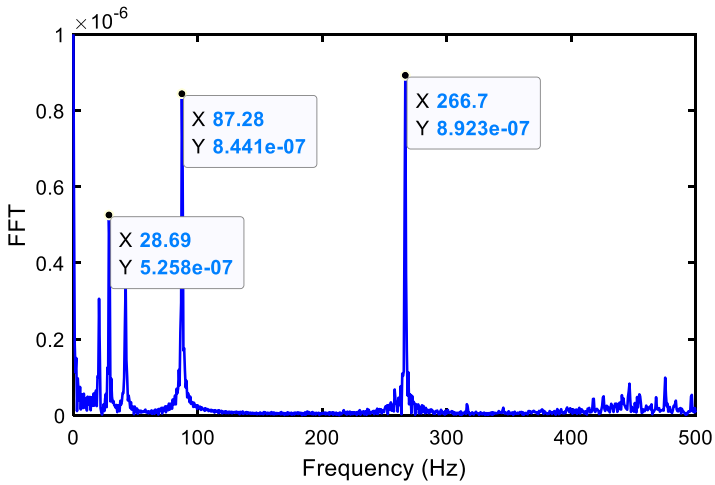

(c) Frequency response from FE model

Fig. 10 Acceleration of rotor from 0 to 1000 rpm

from Fig. 11c. These peaks may be from internal resonances before attaining the final state.

Further, an integrated thermo-hydrodynamic (THD) analysis of rotor- bearing system is studied. By varying the oil-film viscosities and clearances as a function of temperatures, the pressure distributions and bearing forces are obtained from two-dimensional Reynolds equation. Similarly the effect of the in-phase and out-of-phase unbalance at the disk on the responses of the system is studied.

In-Phase Unbalance (ϕ = 0°)

The time-domain response, orbit and phase plots under different loads and temperatures at the left bearing node at a relatively high shaft speed of 85,000 rpm are shown in Figs. 12, 13 and 14.

It is observed that as the operating condition changes, the amplitudes of response drastically alter. The clearances in both nominal and hot operating conditions influence the system responses considerably. Figure 15 shows the corresponding frequency response plots at both bearings. It is observed that there are two main sub-synchronous components occurring close to the resonant peak.

Component A has a constant amplitude in all the cases, and also its frequency range is constant (i.e., 500–510 Hz). Component A occurs from excitation of the conical mode shapes due to the oil whirl/whip. The frequency and amplitudes in component B are speed-dependent. These identifications are in a manner with the testing and numerical results of previous works [32, 33]. The component C is obtained at 1450 Hz corresponding to the critical speed of the rotor operating at 85,000 rpm in both the cases.

It is observed that under hot and nominal operating conditions, the performance of the turbocharger varies considerably. Clearance changes are not much influencing the component A, whereas components B and C are much influenced by the change in clearance.

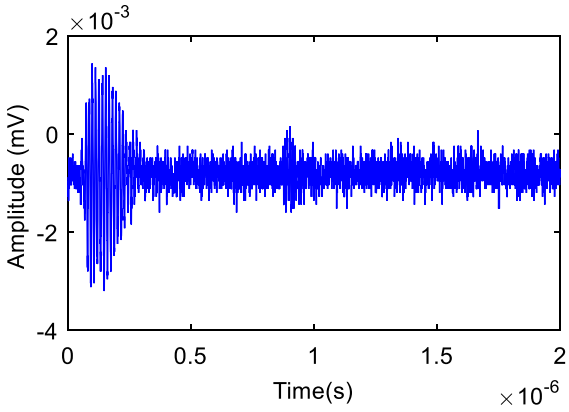

(a) Time history

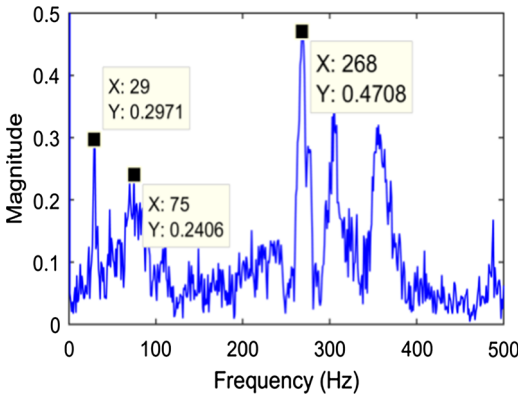

(b) Frequency response from experimental

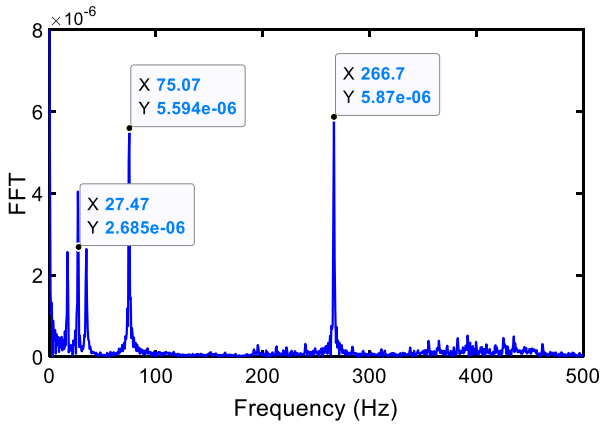

(c) Frequency response from FE model

Fig. 11 Deceleration of the rotor from 1000 to 0 rpm

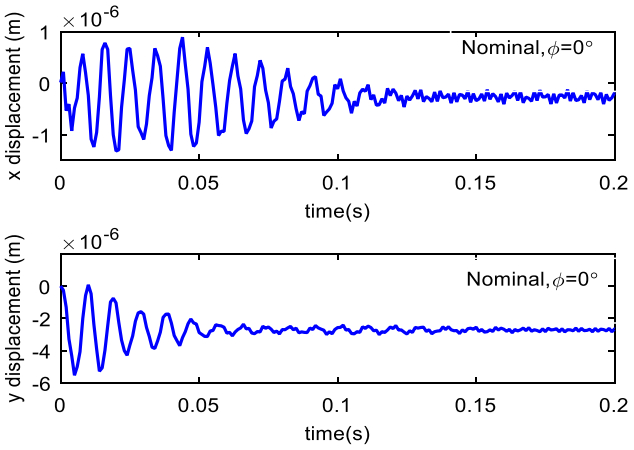

(a) Nominal condition

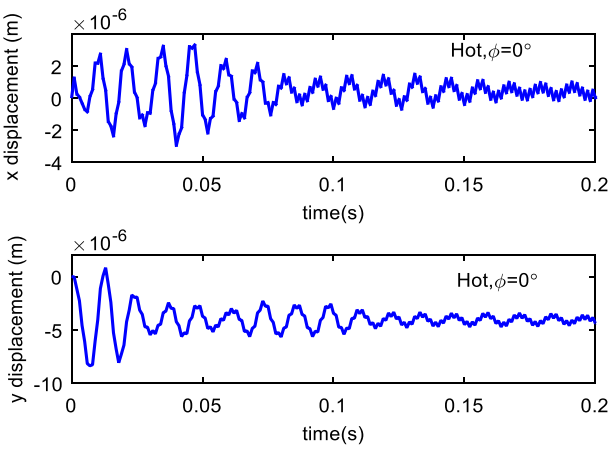

(b) Hot condition

Fig. 12 Time-domain response at left the bearing node

Out-of-Phase Unbalance (ϕ = 180°)

The time-domain response, orbit, and phase plots under different load and temperatures in out-of-phase unbalance condition at the left bearing node with 85,000 rpm are shown in Figs. 16, 17 and 18.

Compared to in-phase unbalance, the out-of-phase unbalance increases the system amplitudes in both nominal

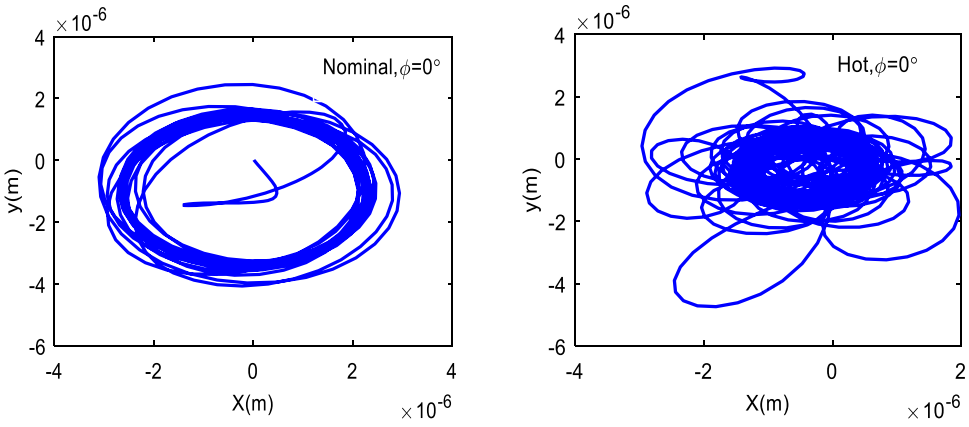

Fig. 13 Orbit plots at left the bearing node

(a) Nominal condition **(b)** Hot condition

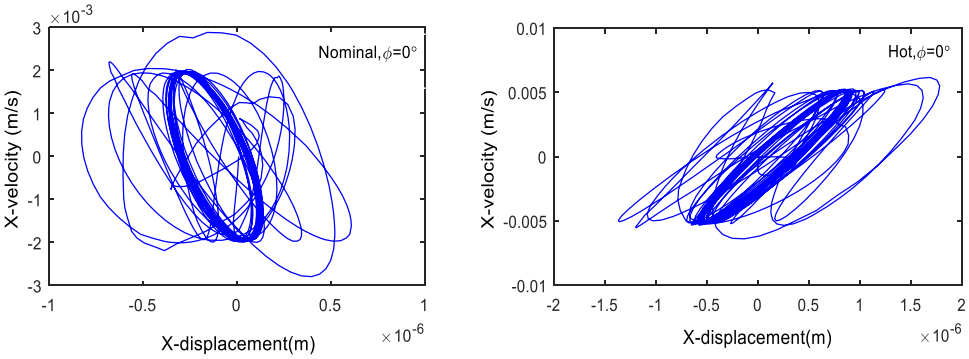

Fig. 14 Phase portraits at left the bearing node

(a) Nominal condition **(b)** Hot condition

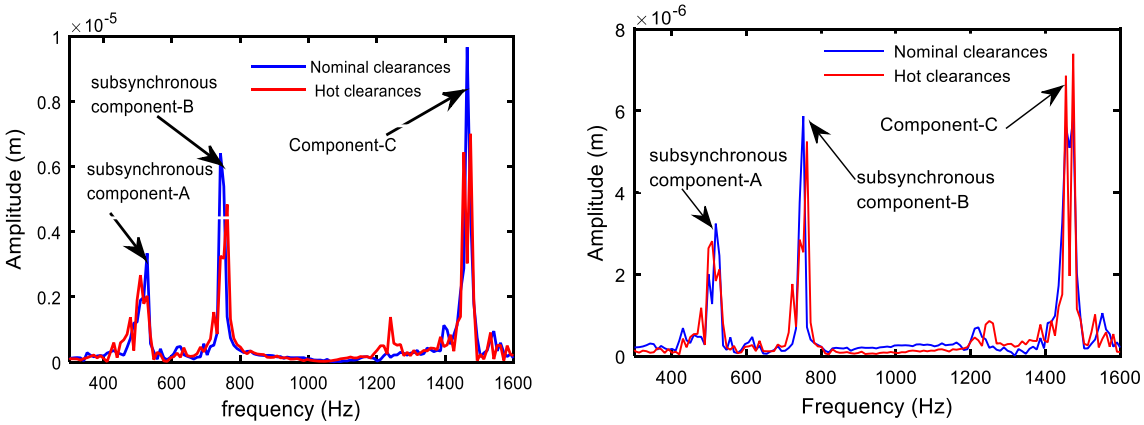

(a) Left side **(b)** Right side

Fig. 15 FFT plots at both bearing nodes at $\phi = 0°$

and hot operating conditions which can be noticed in the time domain response. Figure 19 shows the corresponding frequency response plots at both bearings.

Here, also the component A possesses constant amplitude. It is also observed that under hot and nominal operating conditions the performance of the turbocharger varies. Components A and C are having less amplitude under hot conditions at a phase angle of 180^0. The clearance change has effective influence on the components A and C, while the component B has no much influence.

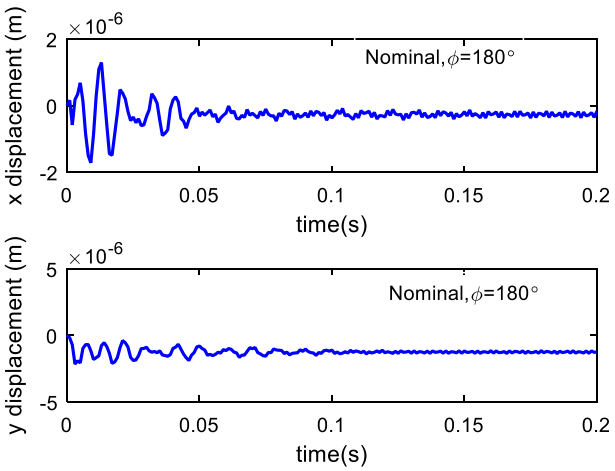

(a) Nominal condition (ϕ=180^0)

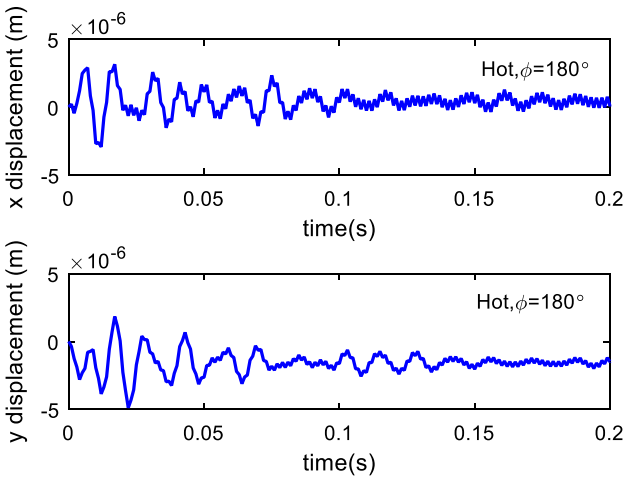

(b) Hot condition (ϕ=180^0)

Fig. 16 Time domain response at left the bearing node

Fig. 17 Orbit plots at left the bearing node

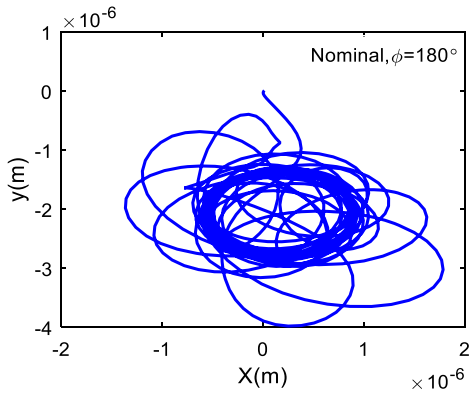

(a) Nominal condition (ϕ=180^0)

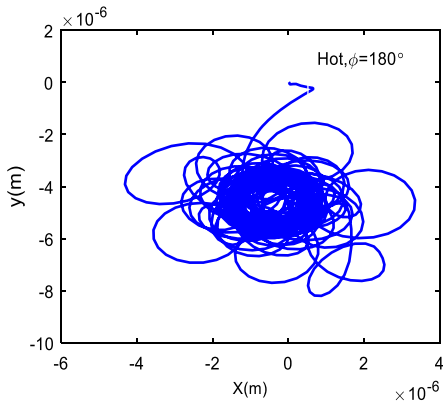

(b) Hot condition (ϕ=180^0)

Fig. 18 Phase portraits at left the bearing node

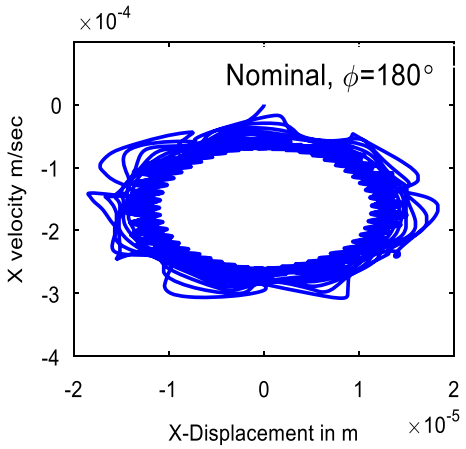

(a) Nominal condition (ϕ=180^0)

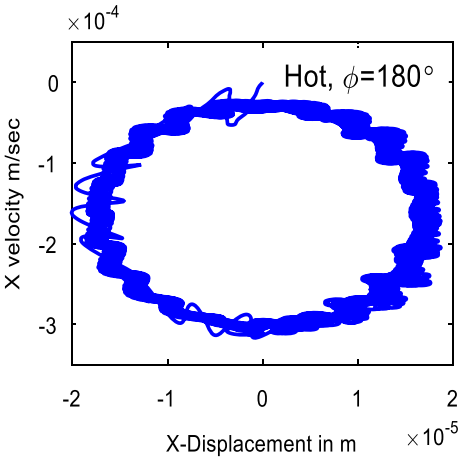

(b) Hot condition (ϕ=180^0)

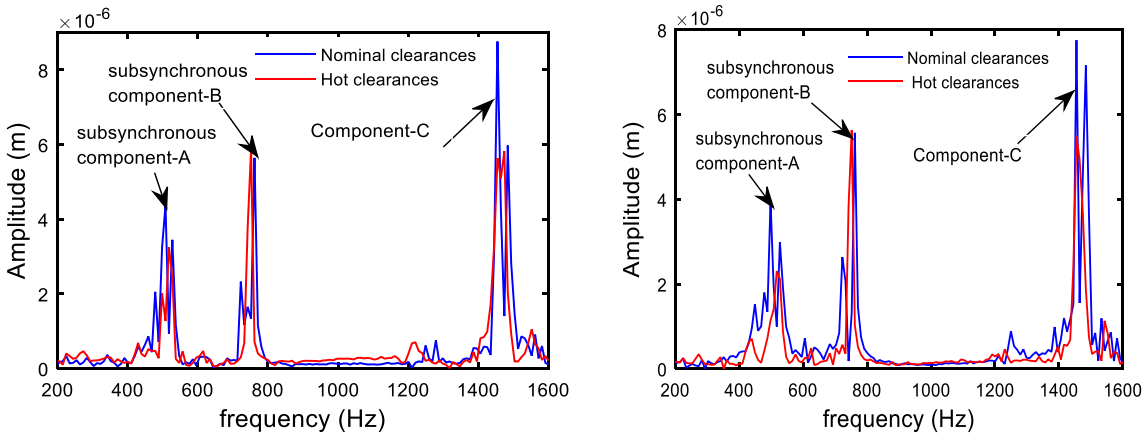

Fig. 19 FFT plots at both bearing nodes at $\phi = 180°$

Conclusions

In the present work, the dynamic analysis of high-speed turbocharger rotor has been studied under transient operating conditions with temperature-dependent lubricant viscosities and film clearance considerations. The present finite element program was first validated with free vibration characteristics using 3-D analysis outcomes. The angular acceleration effects on the stability of the rotor system were then studied, and also the effects of the different load phase angles, temperature and clearances on the rotor system were studied. Transient operation effects at low speed were studied with an experimental setup and outcomes were validated with numerical results. It can be concluded that

- The influence of angular acceleration and deceleration on the overall stability is relatively small.
- For in-phase disk case, the change in the clearances is not much influencing on component A in the frequency response at both bearing nodes, whereas Components B and C are influenced more.
- For out-of-phase case, the change in the clearances is much influencing the components A and C in the frequency response at both bearing node, whereas the component B is not much influenced.
- The static unbalances and the clearance change influences the overall stability of the rotor system.

Combined effect of rotor with temperature dependent viscosity and clearances in transient regime on the overall system dynamics requires further study.

References

1. B. Schweizer, M. Sievert, Nonlinear oscillations of automotive turbocharger turbines. J. Sound Vib. **321**, 955 (2009)
2. B. Schweizer, Oil whirl, oil whip and whirl/whip synchronization occurring in rotor systems with full-floating ring bearings. Nonlinear Dyn. **57**, 509 (2009)
3. L. Tian, W.J. Wang, Z.J. Peng, Effects of bearing outer clearance on the dynamic behaviours of the full floating ring bearing supported turbocharger rotor. Mech. Syst. Signal Process. **31**, 155 (2012)
4. L. Wang, G. Bin, X. Li, X. Zhang, Effects of floating ring bearing manufacturing tolerance clearances on the dynamic characteristics for turbocharger. Chin. J. Mech. Eng. **28**, 530 (2015)
5. H. Zhang, Z. Shi, F. Gu, A. Ball, Modelling of outer and inner film oil pressure for floating ring bearing clearance in turbochargers. J. Phys. Conf. Ser. **305**, 12021 (2011)
6. L.S. Andrés, J. Kerth, Thermal effects on the performance of floating ring bearings for turbochargers. Proc. Inst. Mech. Eng. Part J J. Eng. Tribol. **218**, 437 (2004)
7. S. Tyagi, S.K. Panigrahi, Transient analysis of ball bearing fault simulation using finite element method. J. Inst. Eng. India Ser. C **95**, 309 (2014)
8. A.A. Kozhenkov, R.S. Deitch, Three-dimensional finite element simulation of nonlinear dynamic rotor systems of a turbocharger. J. Vib. Acoust. **130**, 31003 (2008)
9. Y. Zuo, J. Wang, A method for dynamic analysis of three-dimensional solid element rotors with uncertain parameters. J. Eng. Gas Turbines Power **139**, 54501 (2016)
10. J. Suh, A. Palazzolo, Three-dimensional dynamic model of TEHD tilting-pad journal bearing—part I: theoretical modeling. J. Tribol. **137**, 41703 (2015)
11. M.W. Meng, W.J. Jun, W. Zhi, Frequency and stability analysis method of asymmetric anisotropic rotor-bearing system based on three-dimensional solid finite element method. J. Eng. Gas Turbines Power **137**, 102502 (2015)
12. W. Pan, G. Tang, M. Zhang, Modal analysis method for blisks based on three-dimensional blade and two-dimensional axisymmetric disk finite element model. J. Eng. Gas Turbines Power **139**, 52504 (2016)
13. R.D. Burke, C.D. Copeland, T. Duda, M.A. Rayes-Belmote, Lumped capacitance and three-dimensional computational fluid dynamics conjugate heat transfer modeling of an automotive turbocharger. J. Eng. Gas Turbines Power **138**, 92602 (2016)
14. L. Smolík, M. Hajžman, M. Byrtus, Investigation of bearing clearance effects in dynamics of turbochargers. Int. J. Mech. Sci. **127**, 62 (2017)
15. J.R. Serrano, P. Olmeda, F.J. Arnau, M.A. Reyes-Belmonte, H. Tartoussi, A study on the internal convection in small

turbochargers. Proposal of heat transfer convective coefficients. Appl. Therm. Eng. **89**, 587 (2015)
16. G. Li, M. Bao, S. Ding, Y. Li, A system for accurate measuring of thermal-structure displacement on a high speed rotating turbine disk by using digital image correlation technology. Appl. Therm. Eng. **113**, 36 (2017)
17. R.I. Taylor, Tribology and energy efficiency: from molecules to lubricated contacts to complete machines. Faraday Discuss. **156**, 361 (2012)
18. R.I. Taylor, The inclusion of lubricant shear thinning in journal bearing models, in *Tribol. Ser.*, ed. by D. Dowson, M. Priest, C.M. Taylor, P. Ehret, T.H.C. Childs, G. Dalmaz, Y. Berthier, L. Flamand, J.-M. Georges, A.A. Lubrecht (Elsevier, Amsterdam, 1999), pp. 611–619
19. S. Kim, A.B. Palazzolo, Effects of thermo hydrodynamic (THD) floating ring bearing model on rotordynamic bifurcation. Int. J. Non-Linear Mech. **95**, 30 (2017)
20. J. Ferron, J. Frene, R. Boncompain, A study of the thermohydrodynamic performance of a plain journal bearing comparison between theory and experiments. J. Lubr. Technol. **105**, 422 (1983)
21. K.R. Kadam, D.S.S. Banwait, D.S.C. Laroiya, The influence of modified viscosity-temperature equation on thermohydrodynamic analysis of plain journal bearing. Am. J. Mech. Eng. Am. J. Mech. Eng. **2**, 169 (2014)
22. J. Durany, J. Pereira-Pérez, F. Varas, Some aspects of lubrication in heavy regimes: thermal effects, stability and turbulence. Math. Comput. Simul. **102**, 90 (2014)
23. L. San Andrés, V. Barbarie, A. Bhattacharya, K. Gjika, On the effect of thermal energy transport to the performance of (semi) floating ring bearing systems for automotive turbochargers. J. Eng. Gas Turbines Power **134**, 102507 (2012)
24. A. Abdullah, I.S. Mohamad, A.Y. Bani Hashim, N. Abdullah, B.W. Poh, M.H. Md Isa, S. Zainal Abidin, Thermal conductivity and viscosity of deionised water and ethylene glycol-based nanofluids. J. Mech. Eng. Sci. JMES **10**, 2249 (2016)
25. B. Suresh Babu, G. Srinivas, G.V.P.N. Srikanth, Finite element analysis of diffusion effects on convective heat and the mass transfer of two fluids in a vertical channel. Int. J. Automot. Mech. Eng. **14**, 3998 (2017)
26. D.M. Clarke, C. Fall, G.N. Hayden, T.S. Wilkinson, A steady-state model of a floating ring bearing, including thermal effects. J. Tribol. **114**, 141 (1992)
27. M. Deligant, P. Podevin, G. Descombes, CFD model for turbocharger journal bearing performances. Appl. Therm. Eng. **31**, 811 (2011)
28. D.Y. Dhande, D.W. Pande, G.H. Lanjewar, Numerical analysis of three lobe hydrodynamic journal bearing using CFD–FSI technique based on response surface evaluation. J. Braz. Soc. Mech. Sci. Eng. **40**, 393 (2018)
29. S. Weng, W. Tian, H. Zhu, Y. Xia, F. Gao, Y. Zhang, J. Li, Dynamic condensation approach to calculation of structural responses and response sensitivities. Mech. Syst. Signal Process. **88**, 302 (2017)
30. G. Adiletta, A.R. Guido, C. Rossi, Chaotic motions of a rigid rotor in short journal bearings. Nonlinear Dyn. **10**, 251 (1996)
31. D. Tamunodukobipi, I. Emmanuel-Douglas, Y.-B. Lee, Modeling and analysis of floating-ring bearing thermo- hydrodynamic parameters for advanced turbo-rotor systems. Am. J. Eng. Res. **6**, 259 (2017)
32. W.J. Chen, E.J. Gunter, *Introduction to Dynamics of Rotor-Bearing Systems* (Trafford Publishing, Victoria, 2005)
33. K. Ryu, Z. Ashton, Oil-free automotive turbochargers: drag friction and on-engine performance comparisons to oil-lubricated commercial turbochargers. J. Eng. Gas Turbines Power **139**, 1 (2016)
34. Ball Bearings, Precision Miniature Bearings, Industrial Bearings, AST Bearings (2017), https://www.astbearings.com/